JOURNAL OF PROPULSION AND POWER
Vol. 26, No. 3, May–June 2010

Hybrid Reynolds-Averaged and Large-Eddy Simulation of Normal Injection into a Supersonic Crossflow

David M. Peterson* and Graham V. Candler†
University of Minnesota, Minneapolis, Minnesota 55455

DOI: 10.2514/1.46810

Injection through a circular port oriented normally to a Mach 1.6 crossflow is simulated using hybrid Reynolds-averaged Navier–Stokes and large-eddy simulation turbulence models. The simulations compare the performance of two related turbulence models. The standard formulation of the detached-eddy simulation equations is used in the context of a wall-modeled large-eddy simulation. A recently developed derivative of the detached-eddy simulation formulation that was aimed at improving performance when operating as a wall-modeled large-eddy simulation is also used. These methods are used such that the large-scale turbulent structure of the flowfield can be resolved while simulating realistic Reynolds numbers. Simulations are performed on two grids to assess the influence of grid resolution. Comparisons with flowfield visualizations from experiments are used to determine if the proper large-scale structure is being resolved. A thorough validation of the results is performed by comparing with measurements of mean wall pressure from pressure-sensitive paint and measurements of mean velocity and turbulence intensities from laser Doppler velocimetry. Results from the simulations are found to be in good agreement with the experiment.

Introduction

SIMULATING the flow in a real scramjet combustor geometry at the actual operating conditions is a challenging problem. The geometry of the combustor can be quite complex, including features such as cavities, ramps, pylons, and struts. For even relatively simple geometries, the result is a turbulent three-dimensional flowfield with regions of both attached and separated flow, compressible shear layers, and shock interactions. In addition to this, the Reynolds number associated with a scramjet combustor is generally very large. Simulations must be able to accurately capture the mixing and combustion process as well as to provide accurate measures of the skin friction drag. To be useful in scramjet design, the cost of a simulation must remain reasonable such that the simulation can be completed on existing supercomputing clusters, preferably within a few days to a week.

In an effort to build this capability, the present work focuses on a critical aspect of the flowfield in a scramjet combustor: the injection and mixing of fuel. Many injection strategies exist [1], but the focus will be on injection through a normal circular injector flush with the combustor wall. This configuration has been studied for many decades, both analytically and experimentally [2–14]. The schematics in Fig. 1 show some of the key features of the mean flowfield. The details of these flow features have been discussed in the literature.

The flowfield around such an injector is highly unsteady. The shear layer between the jet plume and freestream is dominated by large-scale coherent structure that persists far downstream, as seen in Mie scattering images [7,8,11] and high-speed schlieren images [14]. The turbulent structure results in a jet plume that at any instant in time is highly distorted with regions containing injectant fluid that are separated from each other by unmixed freestream fluid.

Reynolds-averaged Navier–Stokes (RANS) simulations have been used to study the injection flowfield, with the studies of Sriram and Mathew [15], Srinivasan and Bowersox [16], and Viti et al. [17] being recent examples. Such simulations are relatively inexpensive and capture many of the mean flow features. However, RANS simulations do not include the unsteady structure of the jet plume and rely on models to capture mixing and combustion processes.

With computer power continually increasing, it is becoming possible to simulate the flow in a scramjet combustor using large-eddy simulation (LES). This allows for the largest turbulent structures to be resolved. However, the Reynolds number of the flow makes it too costly to properly resolve the near-wall region with LES. LES was used by von Lavante et al. [18] to simulate hydrogen injection and combustion. They were able to resolve some large-scale turbulent structure, but they were limited to a small grid size for three-dimensional flow. Kawai and Lele [19] used LES to study the mixing mechanisms of the injection flowfield, while greatly reducing the flow Reynolds number to resolve the wall. To simulate the real flow conditions, some kind of wall-modeled LES (WMLES) is necessary.

It may also be to our advantage to further restrict the regions in which we are using LES. RANS may not be ideal for separated flow regions or regions where mixing and combustion occur, but it provides an accurate representation of the mean velocity and thermodynamic field in attached boundary layers and requires much less resolution than LES. What would be ideal is a hybrid RANS/LES methodology that allows for side-by-side regions of RANS and WMLES.

One possible WMLES methodology [20] is to use detached-eddy simulation (DES) [21]. WMLES is not the original intention of DES, but as a wall model it is simple and robust [22,23]; thus, it will serve as the starting point for the present simulations. Recently, a DES-based model with use as a WMLES in mind has been developed to address some known issues when using the standard DES formulation in the context of WMLES [24,25]. This model, referred to as *improved delayed detached-eddy simulation* (IDDES), also allows for side-by-side regions of RANS and WMLES, without the need for user-specified zonal definitions, as is the case for the standard formulation of DES [26]. The use of the IDDES model will also be investigated here.

Few WMLES strategies have been applied to the supersonic injection flowfield. Boles et al. [27,28] used a time-dependent blending of RANS and a Smagorinsky-type LES. They qualitatively compared simulation results with plots of mean Mie scattering image intensity and with the standard deviation of the image intensities. Quantitative comparisons were made with mean pressure profiles and mean mixing from Raman scattering. Srinivasan and Bowersox

Received 21 August 2009; revision received 20 November 2009; accepted for publication 20 November 2009.

*Ph.D. Student, Department of Aerospace Engineering and Mechanics. Student Member AIAA.

†Professor, Department of Aerospace Engineering and Mechanics. Fellow AIAA.

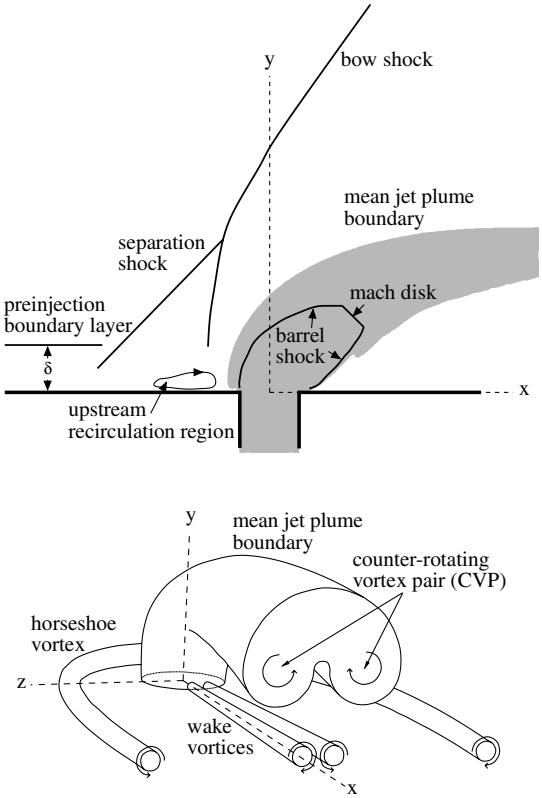

Fig. 1 Schematic of key mean flow features along centerline of jet (top) and perspective view of major vortical structures in the mean (bottom). Freestream flow is in the direction of positive *x*.

[16] used the detached-eddy simulation formulation to handle the blending of RANS and LES modes. They focused on describing the secondary flow structures of the flowfield and made some comparisons to surface oil-flow visualizations and measured pitot pressure.

In this paper, the standard DES and the IDDES formulations are used to simulate the flowfield around a single circular injector oriented normal to the supersonic crossflow. The goal is to determine if the simulations can capture the dominant physics of the flow to a level suitable for analysis, design, and optimization of real scramjet-powered vehicles. Comparisons with flowfield visualizations from the experiment will determine if the simulations can capture the large-scale turbulent structure of the instantaneous flowfield. To determine if the structure resolved by the simulations is physically meaningful, the results from simulations are thoroughly compared with available mean and fluctuating velocity data and mean wall pressure. The effects of grid resolution and differences between the two turbulence models are also examined.

Test-Case Details

The simulations presented here correspond to a set of experiments that investigate normal injection from a circular port into a supersonic crossflow. Santiago and Dutton [9] used a laser Doppler velocimeter (LDV) to measure mean velocity and turbulence intensities. Wall pressure measurements were made using pressure-sensitive paint (PSP) by Everett et al. [10]. VanLerberghe et al. [11] used planar laser-induced fluorescence (PLIF) from acetone to visualize the instantaneous flowfield structure.

The stagnation pressure of the freestream was 241 kPa, with a stagnation temperature of 295 to 300 K. The facility nozzle accelerated the flow to Mach 1.6. Air was injected through a single circular injector with a diameter of $d = 4$ mm. The total pressure and temperature of the injectant was set to 476 kPa and 300 K, respectively. These conditions result in a jet-to-freestream momentum-flux ratio of 1.7.

The preinjection boundary layer was measured using an LDV. The thickness of the preinjection boundary layer was found to be 3.1 mm, or 0.78 injector diameters, at a location five injector diameters upstream of the injector port.

The coordinate system used has its origin at the center of the exit plane of the injector. The x axis points in the streamwise direction and the y axis points in the wall-normal direction. The z axis completes the right-handed coordinate system.

Simulation Methods

Numerical Scheme

Numerics are crucial for capturing the large-scale turbulent structure of the injection flowfield. The dissipation of any scheme cannot be allowed to overwhelm the actual flow physics, yet the scheme used must be robust, reliable, and numerically stable in the presence of shock waves and sharp gradients. We also require that any scheme used be compatible with an unstructured grid framework. This is because an unstructured grid framework provides flexibility in the grid generation that will allow us to make efficient use of grid cells and to include complex geometric features without compromising grid quality. In practice, this limits possible schemes to those with small stencils.

To meet these requirements, the US3D flow solver is used. US3D solves the compressible Navier–Stokes equations using a hybrid structured/unstructured cell-centered finite volume approach. The numerics used in the solver are summarized here; for more detail on the solver, see Nompelis et al. [29].

The inviscid fluxes are evaluated using the modified Steger–Warming flux vector splitting. Evaluation of the fluxes at cell faces using second-order upwind reconstruction has been used with great success when simulating steady-state supersonic and hypersonic flows, but it is too dissipative to allow turbulence to be generated and sustained in LES applications. A third-order upwind-biased flux reconstruction is used here. The third-order upwind-biased reconstruction is still robust but is not overly dissipative. The viscous fluxes use gradients calculated via a weighted least-squares approach.

Time integration in the solver is backward Euler and formally first-order-accurate. The time steps used are small enough that using a formally second-order-accurate time integration scheme was not found to significantly alter the results. The solver uses the full-matrix point relaxation method [30], which is fully implicit. This removes the impractical time-step limitation of explicit methods, particularly on grids with tight boundary-layer clustering, as are used in the present simulations.

Turbulence Modeling

The approach taken for simulating the injection flowfield is to use a hybrid RANS/LES methodology. For some of our simulations, the blending of the RANS and LES portions of the method will be determined by the standard DES equations [21], now referred to as DES97. The one-equation Spalart–Allmaras model [31] with the density corrections of Catris and Aupoix [32] is used as the background RANS model for DES. We are not using the DES equations in the natural mode, where the boundary layers are very thin compared with the wall-parallel spacing of the grid, such that they are fully within the RANS portion of the simulation. Instead, we are using the DES equations as a WMLES, where the RANS portion acts as a wall model for the LES portion. To reduce the simulation cost, we would also like to use the RANS portion of the model throughout attached boundary layers in regions where mixing of fuel and air does not occur. There are, however, some known issues when using DES in this way.

DES97 was first investigated as a wall model for LES by Nikitin et al. [22]. In the channel flow simulations of Nikitin et al., they identified the log-layer mismatch in which a velocity jump occurs between the modeled and resolved portions of the log layer at high Reynolds numbers. The consequence of the velocity jump is underprediction of the skin friction.

Another issue is maintaining RANS behavior in attached boundary layers where the grid is fine in the wall-parallel direction. In DES97, RANS and LES regions are determined only by the grid spacing. The more refined the grid becomes, the closer to the wall the switch moves. Thus, on grids with wall-parallel spacing much smaller than the boundary-layer thickness, DES97 switches to LES mode within the boundary layer. This reduces the eddy viscosity levels in the boundary layer below those needed to maintain proper RANS behavior and can lead to the phenomenon referred to as grid-induced separation [33].

Recently, the delayed detached-eddy simulation (DDES) method was developed to allow for RANS behavior to be maintained inside of attached boundary layers regardless of the wall-parallel spacing [23]. This is accomplished by replacing the RANS/LES switch with a new formulation that makes the switch a function of not only the grid, but also of the local solution. If the eddy viscosity is large and no LES content (resolved velocity fluctuations) is present, the model operates in RANS mode, even if the grid is very fine. DDES, however, is still intended for natural DES applications, primarily external flowfields. DDES can also be used as a WMLES, but, as it was not developed specifically for WMLES, it does not solve the problem of log-layer mismatch.

Interest in using the DDES concept for WMLES applications led to further improvements to the formulation that were aimed at resolving the issue of log-layer mismatch [24,25]. The formulation containing these improvements is referred to as IDDES. For brevity, the details of the model will not be repeated here and the reader is referred to the papers by Travin et al. [24] and Shur et al. [25]. Simulations presented here will also make use of IDDES. No changes to any of the functions or constants contained within the IDDES model have been made for the current study. It should be noted, however, that the model was calibrated using low-speed incompressible flow. Thus, the IDDES model may not be optimized for the high-speed compressible flow we are investigating.

Inflow Boundary Condition

In actual scramjet combustors and most experimental facilities, a boundary layer develops upstream of the injector. This boundary layer can be treated in many ways in a simulation. The simulation could use a mean RANS boundary-layer profile with no turbulent structure or could include turbulent structure by using recycling/rescaling methods [34] or some sort of synthetic inflow generation [35].

Including boundary-layer structure in the inflow might be the preferred method, but could be expensive and difficult to implement in complex geometries. The simplest approach is to use a mean profile obtained from a separate RANS simulation of the relevant geometry. For the RANS profile to be a valid approach, the turbulent structures inside of the boundary layer cannot play an important role in the jet dynamics. Furthermore, without LES content supplied by the user via the boundary conditions, LES content must be able to develop within separated regions of the simulation on its own.

Our experience shows that for normal circular injectors, a RANS profile can be a sufficient representation of the preinjection boundary layer in situations where the jet exit region is well resolved and the jet plume penetrates well above the boundary layer. This is because a large and energetic separation region exists upstream of the injector in the case of normal injection through a circular port. The interaction between the unsteady structure in this separation region and the jet plume generates turbulent structure in the jet shear layer that breaks down the jet plume. Adding turbulent fluctuations to the boundary layer using a synthetic inflow generation method in DES97 simulations was not found to significantly impact the size or shape of test-case jet plumes [36]. Some quantitative differences were seen in the resolved turbulent kinetic energy and mean mixing between simulations with and without the synthetic inflow, but the results without the synthetic inflow were still found to compare favorably with experimental measurements. Using a RANS profile may not be suitable for other injector geometries or orientations, however, as low-angled injection through a circular port has been found to be more sensitive to the inflow condition [36].

All of the simulations presented in this paper will use a mean profile from RANS for the inflow boundary condition. The contour of the facility nozzle was not known, and thus a flat-plate simulation was used to generate the profile. The profile was extracted from a location where the boundary-layer thickness was found to match that of the experiment.

Grid Generation

Grid generation is of critical importance when simulating scramjet fuel injection. High resolution is necessary in the jet shear layer in order to capture the turbulent breakdown of the jet plume as it mixes with the freestream gas. This is of particular importance near the injector port exit, where the jet begins to break down. This high resolution cannot be carried into other regions of the domain, however, as the total cell count could make the calculation prohibitively expensive. In addition to the resolution requirements, a high level of isotropy is desirable for the LES regions of the grid [37], which comprise a large portion of the total element count. Any changes in the spatial resolution of the grid must occur smoothly.

The grids used in this work are generated using the commercial grid generation software GridPro [38]. Although the solver is built with an unstructured grid framework, the grids used for the present simulations do not contain tetrahedral or prismatic elements. They are composed entirely of hexahedral cells. This is done because the hexahedral grids are found to provide a higher-quality solution than a tetrahedral grid with a similar total element count. Also, the hexahedral elements are more efficient at filling volume. The unstructured grid framework does, however, allow for an arbitrary level of complexity in the all-hexahedral grid. This allows for the use of advanced grid generation techniques that can handle complex geometries and make efficient use of grid elements, which is an enabling factor in these simulations.

The grids contain a core of high-density cells in the jet region; rapid but smooth coarsening occurs outside of the core region, as seen in Fig. 2. The figure shows a grid with identical topology and relative grid density to the grids used for this study; however, the grid in the figure has been coarsened significantly for clarity. The grid along the walls near the injector port is swallowed into the injector nozzle. The cell density is much higher near the injector exit than in the downstream region. Although not shown in the figure, the grid is stretched to the walls in order to resolve the large gradients in the boundary layer. The first cell off of the wall is within one wall unit.

The domain extends from $-5 \leq x/d \leq 20$ but is only well resolved up to $x/d = 7$, as no measurements were taken downstream

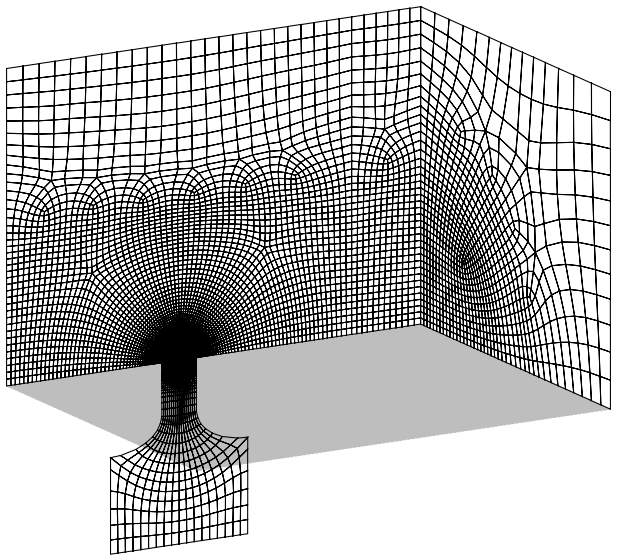

Fig. 2 Slices of the grid along the tunnel centerline and a downstream plane normal to the freestream flow. For clarity, the resolution has been greatly reduced from the levels used in the simulations. The transparent gray plane is the tunnel wall.

of this location. The domain extends to the tunnel walls in the other directions: approximately 9.5d and 8.25d in the spanwise and wall-normal directions. The boundary layer is not resolved on the walls that do not contain the injector. Tests with RANS simulations showed that resolving the boundary layers on those walls did not change the size or trajectory of the jet plume.

The grids extend down into the injector plenum chamber. Typically, the total temperature and total pressure in the plenum chamber are known. Using these values with a characteristic-based subsonic boundary condition has been found to work well when the grid extends down into the plenum, reproducing the proper mass flow rate values for cases in which a value was given [36,39]. If the plenum is not included and only a straight section of injector nozzle is used, the total pressure has to be reduced to achieve the proper mass flow rate. This can be problematic if the mass flow rate through the injector is not known, as is the case with the configuration being simulated here.

In this work, simulations are run using two grid resolution levels. This is done in an effort to determine the grid resolution level required to capture the important features of the flowfield. Comparing solutions on the two grids also allows us to assess the level to which the solution is affected by grid resolution and to ensure that the solutions are not grossly underresolved.

The lower-resolution grid will be referred to as grid A, and the higher-resolution grid will be referred to as grid B. Grid A is composed of 6,588,096 cells. Grid B was created by increasing the grid resolution by a factor of 1.5 in each direction (before boundary-layer clustering) and has 18,624,402 total cells. The time step used was chosen such that the local Courant–Friedrichs–Lewy number remains less than unity in the LES regions of the flow. The time steps used are 0.05 μs on grid A and 0.03333 μs on grid B. Simulations were run on a quad-core AMD Opteron cluster. Grid A was partitioned to run on 64 cores, with grid B on 256 cores. Approximately 83 flow times could be simulated in 24 h of run time for grid A and 67 flow times simulated in 24 h for grid B, where a flow time is defined as the injector diameter over the freestream velocity.

Results

Simulations were performed using both DES97 and IDDES turbulence models on each of two grids with different resolution levels. Each run is started by initializing the flow as a RANS simulation. This allows for the mean flow features, such as shocks and the jet plume, to become established and also to stabilize the mass flow rate, which tends to oscillate for some time due to the shape of the plenum chamber and the way in which the flow is initialized. The simulation is then changed to DES97 mode and run for many flow times (on the order of 50) to allow the unsteady features of the flowfield to develop fully. Only after the flow has been allowed to develop sufficiently are flow statistics accumulated.

The IDDES simulation cannot be started directly from the RANS initialization, as no LES content is introduced through the inflow plane and the model refuses the LES mode. Each IDDES simulation is started from the initialized DES97 simulation, which has LES content that the model recognizes, switching to WMLES mode in the jet-plume region and to RANS in the preinjection boundary layer. Once the flow is established, statistics are taken over 300 flow times.

Grid Resolution Effects

For the simulations to be successful, they must be able to capture the large-scale unsteady features of the flow: in particular, the coherent vortical structures of the jet shear layer. To visualize the vortical structures resolved by the simulations, the second invariant of the velocity gradient tensor Q is used [40]. Figure 3 shows an isosurface of constant Q at an instant in time for the DES97 simulations on grids A and B. The isosurfaces are colored by streamwise velocity. In the figure, flow is from lower left to upper right.

In the top image of Fig. 3, we see that the lower-resolution grid A is capable of resolving large-scale turbulent structure in the jet plume and upstream separation regions. The Kelvin–Helmholtz circumferential rollers discussed by Ben-Yakar et al. [14] are visible in the outer jet shear layer. Other vortex structures can be seen inside of the circumferential rollers. These smaller vortices are produced in the shear layer between the high-speed fluid of the jet plume and the low-speed fluid in the wake immediately behind the jet plume. These vortices have rotation in the opposite sense as the circumferential rollers. Also visible in the figure is the horseshoe vortex that wraps around the injector port, along the wall. The simulation also shows secondary hairpin-shaped vortices that wrap around the horseshoe vortex and are convected downstream.

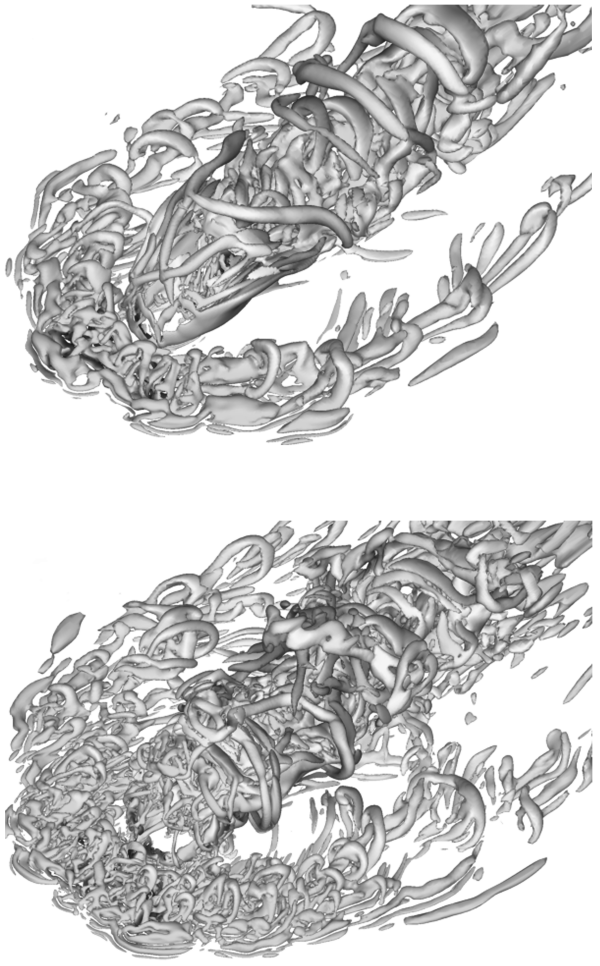

Fig. 3 Surfaces showing a constant value of the second invariant of the velocity gradient tensor. The surfaces are colored by streamwise velocity. The image on the top shows the DES97 simulation on grid A, and the image on the bottom shows the DES97 simulation on grid B.

The lower image in Fig. 3 shows an instant in time for the DES97 simulation on grid B. The larger range of scales that is resolved on the finer grid is immediately apparent in the figure. The shear-layer structures that are clearly identifiable on the coarser grid are still present on the finer grid; however, smaller turbulent structures obstruct and distort them. More structure is also seen in the separation region upstream of the injector and around the horseshoe vortex.

The difference in the turbulent structure resolved by the two grids is further illustrated by looking at isosurfaces of injectant mass fraction, as shown in Fig. 4. The surfaces of Fig. 4 are from the same instant in time as the surfaces of Q shown in Fig. 3 and show a mass fraction value of 0.7. Again, the large structures of the jet shear layer are seen at both resolution levels, but the jet plume has finer structure on the more resolved grid, particularly in the vicinity of the injector exit.

Although not shown, similar structure is resolved for the IDDES simulation on grid B as was shown in Figs. 3 and 4 for the DES97 simulation on grid B. The IDDES simulation on grid A did not, however, produce similar structure to the DES97 simulation on grid A. This is because of the RANS boundary layer used as the

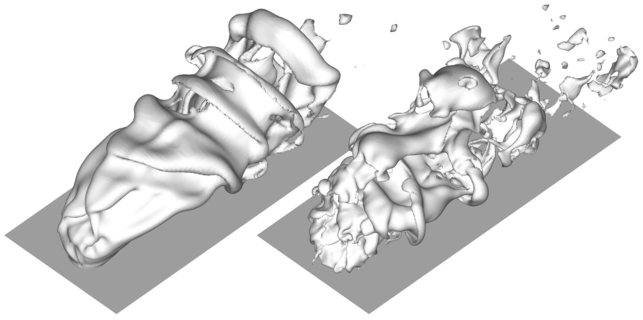

Fig. 4 Surface showing a constant value of injectant mass fraction for the DES97 simulations on grid A (left) and grid B (right).

inflow condition. IDDES maintains RANS behavior in the boundary layer up to the point where LES content develops in the separation region upstream of the injector. At the lower-resolution level of grid A, the encroachment of the RANS mode into the separation region prevented development of such LES content. Without turbulent structure in the separation region upstream of the injector, the jet plume did not break down properly.

To understand how the resolved length-scale range of the instantaneous flowfield affects the mean simulation results, contours of time-averaged streamwise velocity and turbulent kinetic energy are shown in Fig. 5 for the DES97 simulations on the two grids. The streamwise velocity has been normalized by the freestream value, and the same form of dimensionless turbulent kinetic energy (TKE) used by Santiago and Dutton [9] is used here (brackets indicate averaged quantities):

$$\mathrm{TKE} = (\langle u'u' \rangle + \langle v'v' \rangle + \langle w'w' \rangle)/(2U_\infty^2)$$

The plane shown is normal to the freestream at the location $x/d = 5$. The mean results on the two grids are quite similar. Small differences are seen in the plume height and the area around the local velocity minimum within the jet plume. The area under the mean streamwise velocity contour with a normalized value of 0.7 is larger and stretched more in the wall-normal direction on grid A than on the more refined grid B. However, the mean streamwise velocity magnitudes in the jet plume differ by less than 0.05 U_∞ between the two simulations.

Grid B resolves more instantaneous structure, as seen in Figs. 3 and 4, but this does not result in significant differences in the mean resolved TKE in the jet plume. The peak value of TKE in the jet plume is found to be located slightly higher in the grid A simulation than the finer grid B simulation, but the peak values are within 3.5% of each other. There is a significant difference in the peak magnitude of TKE found in the wake vortices located below the jet plume. There, the value of TKE on the finer grid B is 36% higher than the value found on grid A. This indicates that the near-wall region may be underresolved in the simulation on grid A.

Turbulence Model Effects

Figure 6 shows a comparison between the mean streamwise velocity and the nondimensional TKE of the DES97 simulation on grid B and the IDDES simulation on grid B. We see only minor differences in the jet plume of the two plots. The plume height, width, and shape are the same for both simulations. Only small quantitative differences in TKE and velocity are found. The peak value of TKE for the IDDES simulation is less than 3% larger than the peak of the DES97 simulation, and both peaks occur at about $y/d = 1.6$. The contour surrounding the local velocity minimum in the jet plume is somewhat larger in the IDDES simulation, but the values of the local minima are within 0.002 U_∞ and both are close to $y/d = 1.15$.

Some differences are seen in the plots at the wake vortices between the jet plume and the wall. Values of TKE and streamwise velocity are similar in the wake vortex region, but the center of the vortex is found to be around $0.15d$ farther from the centerline in the IDDES simulation. We also see larger mean streamwise velocity near the wall, between the vortex and centerline, in the IDDES simulation.

The most visible difference between the DES97 and IDDES simulations is found in the separation region upstream of the injector port. This is illustrated by the plots shown in Fig. 7. The plots show instantaneous contours of temperature, which visualizes the separation region, particularly by taking note of the position of the

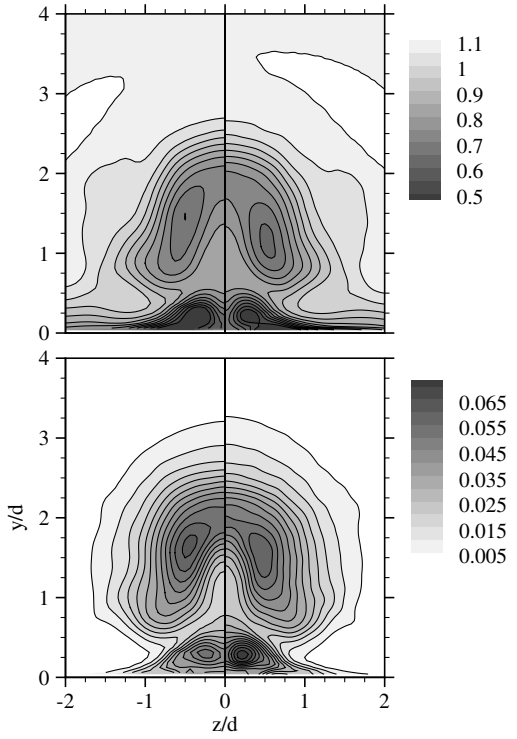

Fig. 5 Mean streamwise velocity (top) and nondimensional TKE (bottom) at the plane $x/d = 5$. The left half of each plot shows DES97 on grid A, and the right half shows DES97 on grid B.

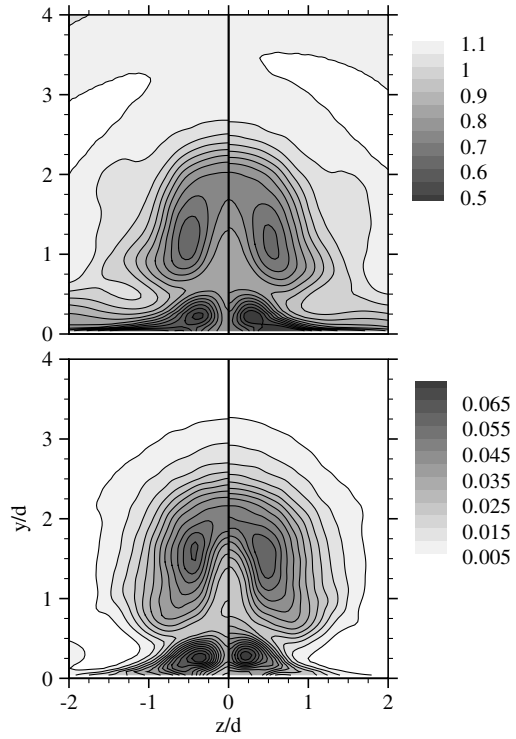

Fig. 6 Mean streamwise velocity (top) and nondimensional TKE (bottom) at the plane $x/d = 5$. The left half of each plot shows IDDES on grid B, and the right half shows DES97 on grid B.

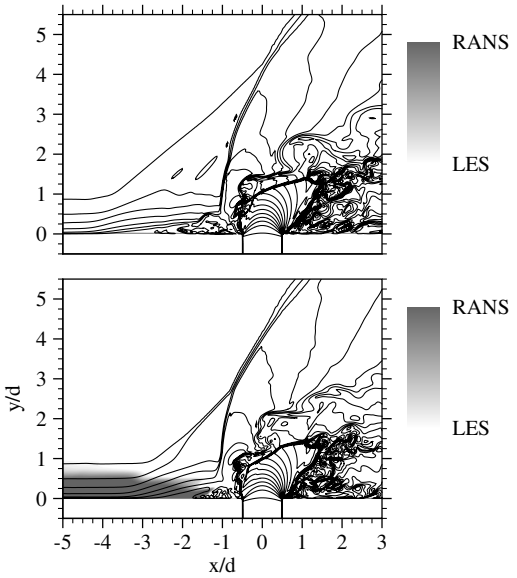

Fig. 7 Lines showing temperature contours on tunnel centerline for DES97 simulation on grid B (top) and IDDES simulation on grid B (bottom). Grayscale shading shows switch between RANS and LES modes.

separation shock. In addition to temperature, the plots show the switch that determines RANS and LES regions for each model. The darkest regions indicate pure RANS, and white regions indicate LES.

It is seen that separation occurs more than one diameter farther upstream in the DES97 simulation than in the IDDES simulation. The reason for this is modeled stress depletion in the DES97 case. The grid is much finer than the boundary-layer thickness in this region of the domain; thus, the switch from RANS to LES occurs deep within the boundary layer. The RANS portion of the DES97 simulation is barely visible in Fig. 7. This causes the eddy viscosity levels from the RANS boundary-layer profile that is read into the inflow plane of the domain to be reduced to levels far below what is needed to maintain the RANS profile. The consequence is that the skin friction drops, causing premature separation of the preinjection boundary layer. The formulation of IDDES prevents this premature separation from happening. The model sees the high eddy viscosity levels from the inflow RANS profile and, at the same time, a lack of LES content. Thus, RANS mode is maintained to the location where LES content has developed in the separation region, as seen in Fig. 7. In this way, IDDES is performing as expected and allows for side-by-side regions of RANS and WMLES.

Comparison with Experimental Data

In the following section, comparisons are made between simulation results and experimental visualizations and measurements. Given the similarity between the DES97 and IDDES results in the jet plume, as well as the similarity between the DES97 results on grids A and B, direct comparisons will be made primarily between the IDDES simulation on grid B and the experiments. The exception will be in comparing with the measured wall pressure, as this is where the most significant differences between the DES97 and IDDES simulations are found.

PLIF Flowfield Visualization

In the work of VanLerberghe et al. [11], acetone PLIF was used to capture instantaneous images of a sonic jet in a supersonic crossflow. Side-view images of the jet plume were gathered along the centerline of the tunnel, as well as images of jet cross sections located two injector diameters downstream of the injector. In the side-view images displayed in Fig. 8, the large-scale turbulent structure of the

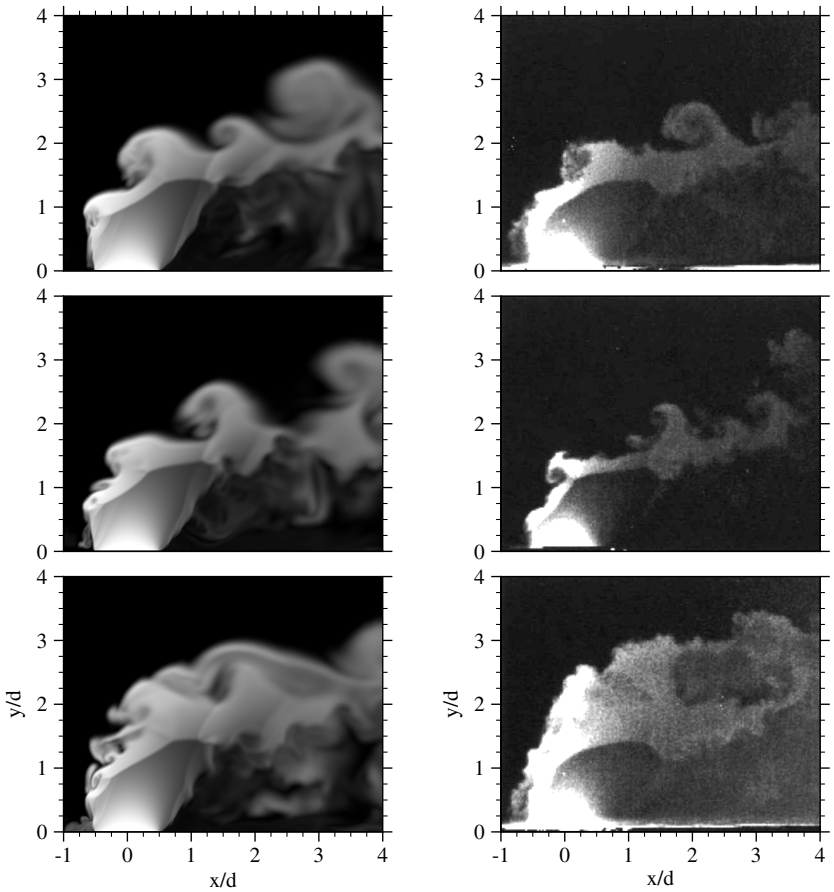

Fig. 8 Representative instantaneous images along tunnel centerline. The IDDES simulation on grid B is shown in the left column, with contours shaded by square-root of density. PLIF images from [11] are shown in the right column.

jet shear layer is clearly visible. The upper edge of the jet plume is dominated by vortices that wrap around the jet shear layer, rotating in a counterclockwise direction when viewed with the freestream moving from left to right, due to the higher velocity of the jet fluid compared with the freestream fluid that passes through the bow shock.

Figure 8 also shows instantaneous images along the centerline from the IDDES simulation on grid B. The images are colored by the square root of injectant density, with white indicating the highest levels and black indicating zero injectant. The square root of the density is used because it makes more detail visible at the lower density levels. The large vortices of the upper shear layer are clearly visible in the simulation images. Consistent with the experimental PLIF images, there is great variation in the size and frequency of the vortices seen in the simulation. Occasionally, a large mass of injectant fluid with less coherent structure is seen in the upper part of the jet shear layer, as in the bottom simulation image of Fig. 8. Such instances are generally found to occur when there is significant interaction between large turbulent structure in the upstream separation region and the windward side of the jet plume.

The barrel shock and Mach disk are also visible in the images of Fig. 8. The flow coming out of the injector rapidly expands to low density, making the barrel shock appear as a region of low intensity. As observed in the experiment, the windward side of the barrel shock is found to be unsteady. The rolling structures of the upper jet shear layer flatten out portions of the curved barrel shock.

Instantaneous images from the simulation and the experiment that show a jet cross section at $x/d = 2$ are displayed in Fig. 9. The images from the simulation display a large variation in the size and shape of the jet-plume cross section, as do the images from the experiment at the same location. Also visible in the images of Fig. 9 is the freestream fluid being drawn up into the center of the jet plume from below by the rotation of the counter-rotating vortex pair (CVP). Images from the experiment reveal the presence of mushroom-shaped structures that extend out from the outer jet-plume boundary. Similar structures are seen in the simulation images as well. The presence of this mostly streamwise-oriented rotation in the jet shear layer is also visible in the three-dimensional views of the jet plume, showing the second invariant of the velocity gradient tensor and the injectant mass fraction in Figs. 3 and 4.

Mean Wall Pressure

Figure 10 shows the mean wall pressure along the centerline of the tunnel for the IDDES simulation on grid B, the DES97 simulation on grid B, and the PSP measurements of Everett et al. [10]. The location of boundary-layer separation upstream of the injector is identified by a sudden rise in pressure. Separation occurs farther upstream in the DES97 simulation than in the IDDES simulation. The reasons for this premature separation were discussed earlier.

The pressure rise in the separation region upstream of the injector port is captured well by IDDES. The pressure peaks at around $p/p_\infty = 1.5$ near $x/d = -2$ in the experiment, with similar values predicted by IDDES. The DES97 simulation predicts a peak of $p/p_\infty = 1.3$ at about $x/d = -3$. Both simulations capture the sharp rise in pressure just upstream of the injector, with peak pressure values larger than seen in the experiment.

Immediately downstream of the injector port, the two simulations predict nearly identical pressure profiles. Both simulations reproduce the location and magnitude of the pressure minimum downstream of the injector. It is not until three diameters downstream that the two simulations begin to diverge from each other. Downstream of $x/d = 3$, the pressure in the IDDES simulation begins to rise more rapidly than the DES97 simulation. The pressure in the IDDES simulation briefly rises above $p/p_\infty = 1$, before settling back near $p/p_\infty = 1$ in the far field. The pressure in the experiment and the DES97 simulation both remain below $p/p_\infty = 1$ in this region. Beyond $x/d = 6$, the profiles from the two simulations are once again nearly identical.

Mean Velocity

Profiles of mean streamwise and wall-normal velocity components at several stations downstream of the injector port are shown in Fig. 11. The profiles are positioned along the tunnel centerline

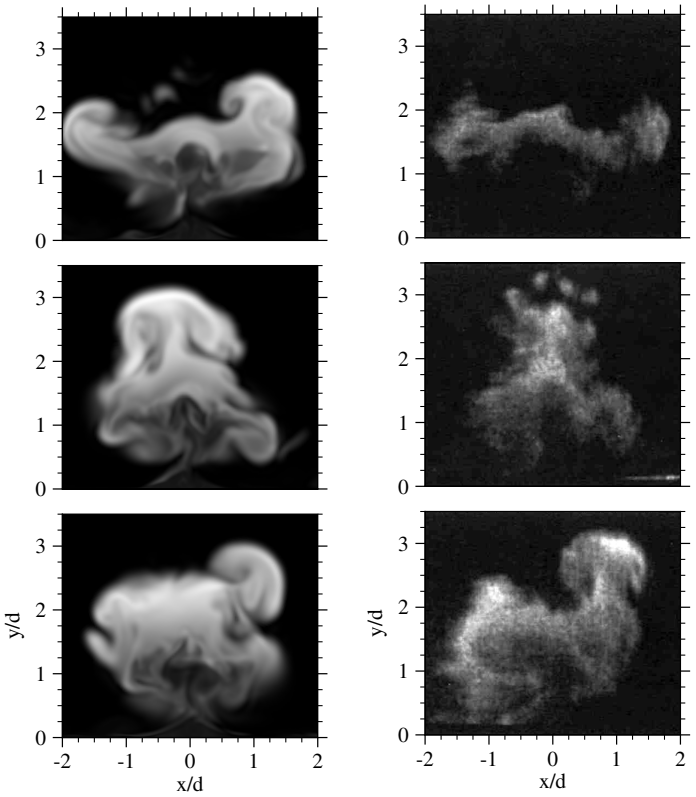

Fig. 9 Representative instantaneous images at the plane $x/d = 2$. The IDDES simulation on grid B is shown in the left column, with contours shaded by square-root of density. PLIF images from [11] are shown in the right column.

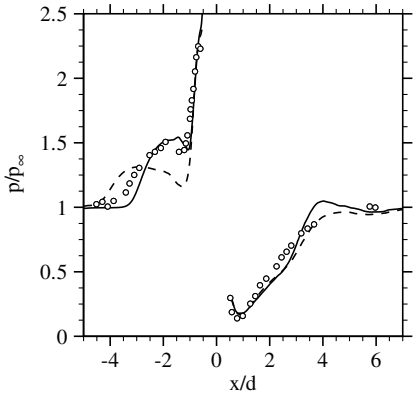

Fig. 10 Mean wall pressure along tunnel centerline. Symbols show experimental data, solid line shows IDDES simulation on grid B, and dashed line shows DES97 simulation on grid B.

($z/d = 0$) at downstream locations of $x/d = 1$, 3, 5 and 7. In the figure, the velocities have been normalized by the freestream velocity. The scales of each of the four axes in each plot are identical. The symbols show the LDV measurements from the experiments of Santiago and Dutton [9], and the solid lines show the results of the IDDES simulation on grid B.

The profile at $x/d = 1$ passes through the barrel shock of the jet plume. The streamwise velocity is nearly constant above $y/d = 3$. Below this, the experiment shows a slight increase in streamwise velocity, before a sharp decrease down to $y/d = 1.5$. The nearly linear region is within the barrel shock. Below $y/d = 0.75$, there is again a sharp decrease in the streamwise velocity of the experiment as the profile enters the low-speed wake that is below and behind the barrel shock. The simulation results deviate from the LDV data in the barrel-shock region. The simulation predicts a larger and more constant streamwise velocity within and directly above the barrel shock. Low-speed flow is also found below the barrel shock in the simulation; however, while the velocities in the experiment remain positive, the simulation predicts an area of reverse flow. Agreement within the barrel-shock region is better for the wall-normal velocity. Both the experiment and simulation predict maximum wall-normal velocity greater than the freestream velocity. This maximum occurs in the upper part of the barrel shock.

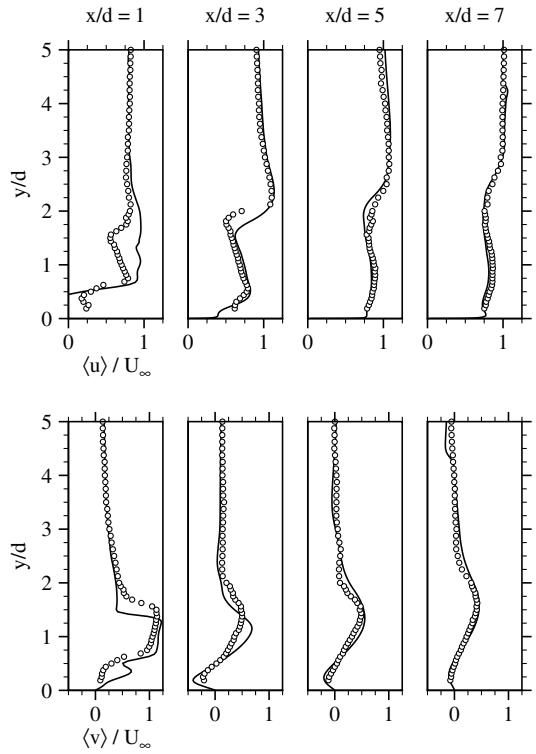

Fig. 11 Normalized mean streamwise (top row) and wall-normal (bottom row) velocity profiles at various downstream locations along tunnel centerline. Symbols show experimental data and solid lines show IDDES simulation on grid B.

The profile at $x/d = 3$ is completely downstream of the barrel shock. The streamwise velocity within the wake of the jet plume is slower than the flow outside of the jet. The shear layer between these two regions is clearly visible around $y/d = 2$. The simulation predicts a slightly thicker shear layer than seen in the experiment. Otherwise, the agreement between the simulation and LDV measurements is very good. The jet plume is also marked by an area of increased wall-normal velocity. This is due to the presence of the counter-rotating vortex pair that forms within the jet plume. The simulation is found to predict a larger maximum wall-normal velocity as compared with the experiment: $0.68U_\infty$ vs $0.5U_\infty$. The maximum occurs at a distance of $1.37d$ from the wall in the experiment and $1.14d$ in the simulation. Near the wall, both the experiment and simulation show flow moving toward the wall below $y/d = 0.48$. This is caused by the wake vortices, which are a strong wall-bounded vortex pair having rotation in the opposite sense of the CVP, drawing flow toward the wall.

As the flow moves downstream, the streamwise velocity within the jet plume approaches that of the surrounding flow, reducing the velocity jump across the shear layer. The shear layer thickens as more fluid is entrained within the jet plume, and it also moves further from the wall. The CVP weakens as the vortices move downstream, resulting in lower peak wall-normal velocity within the jet plume. At $x/d = 5$ and 7, the magnitudes and locations of the peak in wall-normal velocity predicted by the simulation agree well with the LDV data. The wake vortices also weaken as they move downstream; however, small negative wall-normal velocities can still be seen near the walls at $x/d = 5$ and 7 in both the simulation and the experiment. A small jump in each of the velocity components is seen above $y/d = 4$ in the simulation profile at $x/d = 7$, but not in the experiment. The jump in the simulation is caused by the bow shock that has reflected off of the top wall. As the boundary layer is not resolved on the top wall, the shock reflects differently in the simulation than in the experiment.

LDV measurements were also taken in crossflow planes at $x/d = 3$ and 5 in the experiments of Santiago and Dutton [9]. Contours of mean streamwise velocity, as well as vectors showing in-plane velocity, are shown for these two planes in Fig. 12. The right-hand side of each plot shows the LDV data from the experiment. The left-hand side shows results from the IDDES simulation on grid B. The simulation plots were obtained by averaging the two halves of the domain across $z/d = 0$. The simulation results are already quite symmetric, with the maximum difference in mean velocity values between positive and negative z/d locations being less than $0.03U_\infty$. Thus, little is changed by this averaging.

The jet plume is readily visible in the contours of Fig. 12 as an area of lower streamwise velocity. At $x/d = 3$, velocity levels within the jet plume predicted by the simulation are consistent with those seen in the experiment, though the local minimum near the centerline is closer to the wall in the simulation. Using the contour with a non-dimensional velocity value of 1.0, the predicted plume height of $1.98d$ is $0.15d$ less than in the experiment. A more significant difference in the width of the jet plume is seen: $1.24d$ in the simulation vs $0.93d$ in the experiment. Velocity levels in the simulation are also consistent with those in the experiment at $x/d = 5$. At $x/d = 5$, the local minimum in streamwise velocity in the jet plume is located off of the centerline. The value in the simulation is within $0.05U_\infty$ of the value in the experiment; however, the location is approximately $0.5d$ closer to the wall in the simulation. The height of the jet plume is predicted well by the simulation. The width at the top of the simulation jet plume is similar to the experiment; however, the jet plume in the experiment is nearly constant in width, whereas in the simulation it becomes wider at the bottom.

The counter-rotating vortex pair is made visible by the in-plane velocity vectors. In the simulation, the CVP is found to be centered at

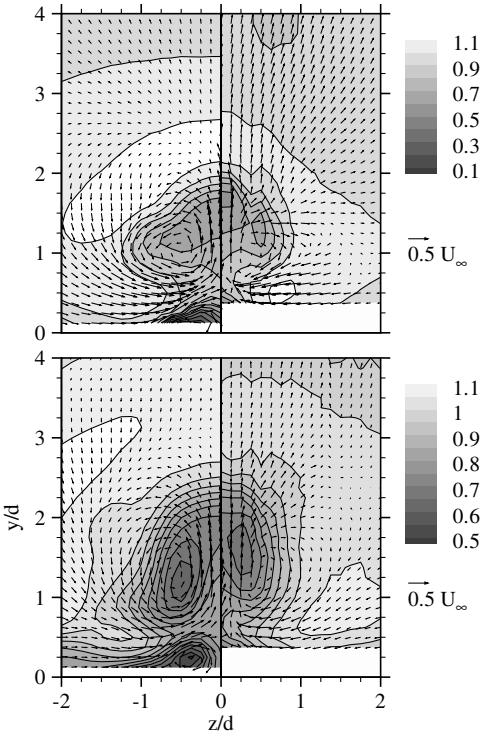

Fig. 12 Mean streamwise velocity contours and in-plane velocity vectors at planes $x/d = 3$ (top) and $x/d = 5$ (bottom). The left half of each plot shows IDDES simulation, and the right half shows LDV data.

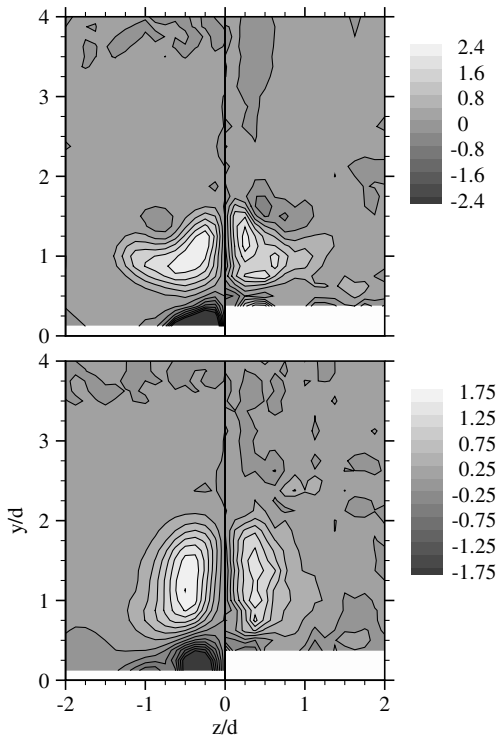

Fig. 13 Normalized vorticity contours at planes $x/d = 3$ (top) and $x/d = 5$ (bottom). The left half of each plot shows IDDES simulation, and the right half shows LDV data.

$z/d = 0.53$ and $y/d = 1.0$ in the $x/d = 3$ plane. The LDV data shows the CVP to be centered at $z/d = 0.34$ and $y/d = 1.0$ in this plane. By the plane at $x/d = 5$, the LDV data shows the CVP to have moved out to $z/d = 0.51$ and up to $y/d = 1.3$. The simulation predicts the same wall-normal location for the center of the CVP, but shows the center to be farther from the centerline at $z/d = 0.60$. The only other vortical structures seen in the two planes are the wake vortices between the CVP and the wall. They are visible in the simulation results, but the LDV measurements did not extend close enough to the wall to fully capture them.

The largest wall-normal velocities in the crossflow planes are found on the centerline between the CVP and were discussed earlier when showing the profiles along the tunnel centerline. The largest spanwise velocities are found below the CVP, where flow is being drawn into the jet plume and is constrained by the wall below. As with the wall-normal velocity, the peak spanwise velocity magnitude is larger in the simulation at $x/d = 3$: $0.61U_\infty$ vs $0.54U_\infty$. Agreement is improved at $x/d = 5$, where both the LDV data and simulation show peak spanwise values of $0.33U_\infty$.

Using central finite differences, the streamwise vorticity was calculated from the mean velocity fields for the two crossflow planes and was normalized using the freestream velocity and injector diameter. For the comparison, the simulation results were interpolated onto the same collection grid as the experiment, with spacing of $0.125d$ in each direction. The results are shown in Fig. 13. As before, the experimental results are shown on the right, with the simulation on the left. We can see that the shape and size of the vorticity contours are predicted well by the simulation at both planes. At $x/d = 3$, the contours take a triangular shape. A small region of vorticity with opposite sign is found above the region of maximum vorticity. A similar region is seen in the simulation, albeit smaller and with reduced magnitude. Peak vorticity in the experiment has a nondimensional value of 2.2, and in the simulation the peak value is 2.4. At $x/d = 5$, being less constrained by the wall below, the vorticity contours take a more elliptical shape, with the centers roughly corresponding to the center of the CVP. The peak magnitude from the LDV data has decayed to a nondimensional value of 1.5. In the simulation, the peak value has dropped to 1.75.

Turbulence Quantities

Turbulence intensities were also measured with the LDV by Santiago and Dutton [9]. Nondimensional TKE contours are shown for the crossflow planes at $x/d = 3$ and $x/d = 5$ in Fig. 14. The right half of each plot shows the TKE measured by the LDV. The left half of each plot shows the resolved TKE from the IDDES simulation on grid B. As before, the simulation data has been averaged across the plane of symmetry.

Qualitatively, the shape of the TKE contours in the simulation is consistent with that seen in the experimental measurements at both planes. At $x/d = 3$, we see trends in the TKE contours similar to those seen for the mean streamwise velocity. The plume heights are similar, but the spanwise width of the contours extend farther from the centerline in the simulation than is seen in the experiment. The quantitative values of TKE in the core of the jet plume at $x/d = 3$ are generally higher in the simulation than in the experiment. The maximum value of nondimensional TKE in the simulation is 0.1, whereas the maximum measured value is 0.075. It should be noted, however, that Santiago and Dutton [9] reported significant asymmetries in turbulence quantities at the $x/d = 3$ plane. Traverses across the centerline of the tunnel showed differences as much as $0.18U_\infty$ in the velocity fluctuations. The simulation results do not show such an asymmetry. The largest differences in the fluctuations across the centerline were no more than $0.025U_\infty$.

Quantitative agreement is improved at the $x/d = 5$ plane. Within the jet plume, the resolved TKE is found to take values very consistent with the experiment. The peak value of nondimensional TKE in the jet plume is found to be approximately 0.61 for both the simulation and LDV data, with the peak value located slightly farther from the wall in the simulation. In the $x/d = 5$ plane, the global maximum in TKE for the simulation occurs in the wake vortices, below the jet plume. The maximum value in this region is 0.75. Only the top portion of the wake vortices was measured in the experimental results.

Plots of the nondimensional Reynolds stress $\langle u'v' \rangle / U_\infty^2$ are shown in Fig. 15 for both crossflow planes. Again, the shapes of the contours from the simulation are qualitatively very similar to the experiment. At both planes, a region of large negative correlation is found in the

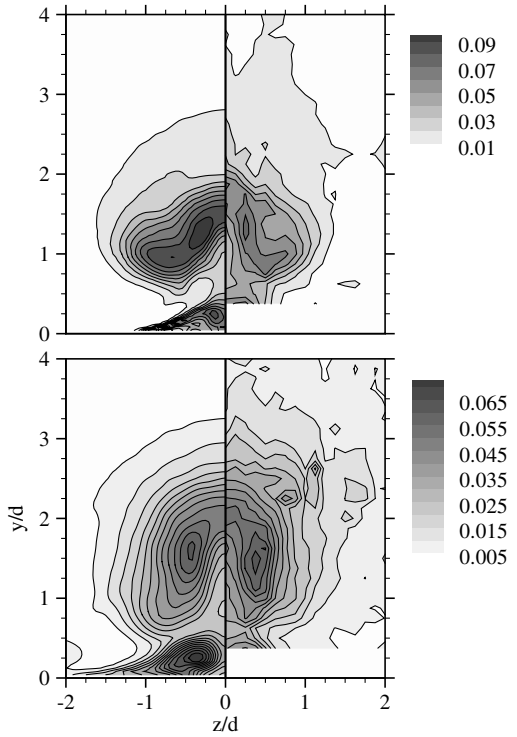

Fig. 14 Normalized TKE contours at planes $x/d = 3$ (top) and $x/d = 5$ (bottom). The left half of each plot shows IDDES simulation, and the right half shows LDV data.

region corresponding to the outer boundary of the jet plume, where the large Kelvin–Helmholtz circumferential rollers are found. The most negative values are found along the centerline. In the experiment at $x/d = 3$, this occurs at $y/d = 1.9$ and has a nondimensional value of -0.03. The peak in the simulation plot is somewhat closer to the wall at $y/d = 1.7$, with a value of -0.024. A region of positive Reynolds stress is found in the lower part of the jet plume, away from the centerline at $x/d = 3$. Here, the values reach 0.016 and 0.009 in the simulation and experiment, respectively. At $x/d = 5$, the region of most negative Reynolds stress has moved up to approximately $y/d = 2.25$ in both the simulation and experiment, with nondimensional values of -0.015 and -0.016. The region of positive Reynolds stress moves toward the centerline and farther from the wall at the $x/d = 5$ plane. It has also become stretched in the wall-normal direction. Along with the local maximum around $y/d = 1.3$, the simulation shows a second local maximum near the lower outer edge of the jet plume at $z/d = 0.75$ and $y/d = 0.65$. Only the local maximum at $y/d = 1.3$ is seen in the experiment.

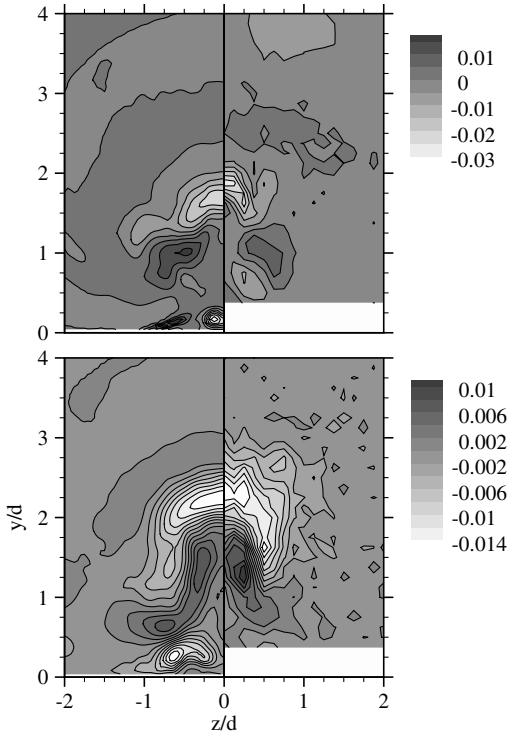

Fig. 15 Normalized $\langle u'v' \rangle$ Reynolds stress contours at planes $x/d = 3$ (top) and $x/d = 5$ (bottom). The left half of each plot shows IDDES simulation, and the right half shows LDV data.

Conclusions

Simulations of injection through a circular injector oriented normal to a supersonic crossflow were performed using the standard detached-eddy simulation formulation (DES97) as well as a more recently developed derivative of DES97, referred to as IDDES. These hybrid RANS/LES turbulence models were used so that the large-scale turbulent structure of the jet-interaction flowfield could be resolved by the LES portion, while the RANS portion functions as a wall model such that the flows can be simulated at realistic Reynolds numbers. All of the simulations used a steady-state boundary-layer profile from a RANS simulation as an inflow condition.

Simulations were performed on two grids of different resolutions. The finer grid had 1.5 times the resolution in each direction of the coarser grid. A larger range of turbulent structure was resolved on the finer grid, but resulting velocity statistics were similar in the jet plume on the two grids. However, when using a mean RANS boundary-layer profile as an inflow condition for IDDES, the encroachment of the RANS mode into the separation region upstream of the injector can prevent unsteady structure from developing in the jet plume if that region is not sufficiently resolved. This highlights the importance of using flowfield visualization to verify that turbulent structure is being resolved in the simulation.

Within the jet plume, the velocity statistics predicted by the DES97 and IDDES simulations on the finer grid reveal only small quantitative differences. The most significant difference in the results was found in the separation region upstream of the injector. Separation was premature in the DES97 simulation, as expected. The result was a poorly predicted wall-pressure profile. IDDES maintained the RANS behavior of the inflow profile and resulted in improved prediction of separation location and wall pressure. This demonstrates the utility of the IDDES model's ability to have side-by-side regions of pure RANS and wall-modeled LES. The improvements in the upstream separation region lead to the recommendation that the IDDES formulation be used over the DES97 formulation when a RANS profile is used as an inflow condition. However, the case investigated here is not a complete test of IDDES for supersonic compressible flow. Further work needs to be done in investigating the use of the model's WMLES capabilities: simulating attached and detached supersonic boundary layers, for example.

Qualitative flow visualizations from the simulations compare well with flow visualizations from experiments. Quantitative comparisons with mean velocity fields were generally good. Comparisons with turbulence measurements were also favorable. The magnitudes and distribution of turbulent kinetic energy resolved in the simulations are consistent with those measured in the experiment, with better quantitative agreement found at the more downstream measurement location. Agreement is also good for the $\langle u'v' \rangle$ Reynolds stress.

The results of this paper show that DES-based turbulence models can be used to accurately simulate the complex jet-interaction flowfield around a normal circular injector. When these models are used in conjunction with high-quality numerics and a grid that is carefully designed to properly resolve key regions of the flow, the important flow physics that result in the first and second-order velocity statistics are captured. Any method must be thoroughly validated against experimental data to gain confidence in the results. The favorable comparisons presented here indicate that for the class of normal circular injectors examined, the methods employed in this

work can be used for predictive capabilities. The methods used in the simulations are efficient, allowing solutions to be obtained in a time frame that is meaningful for engineering analysis. The methods are also scalable, which makes large-scale computations tractable. This gives promise to the prospect of using these type of simulations to predict the performance of complete scramjet combustor sections.

Acknowledgments

The authors would like to thank Juan Santiago and J. Craig Dutton for providing the experimental data. This research is supported by the U.S. Air Force Office of Scientific Research (AFOSR) Multi-disciplinary University Research Initiative (MURI) under grant no. FA9550-04-1-0389 and under grant no. FA9550-04-1-0341. The views and conclusions contained herein are those of the authors and should not be interpreted as necessarily representing the official policies or endorsements, either expressed or implied, of the AFOSR or the U.S. Government.

References

[1] Curran, E. T., and Murthy, S. N. B. (eds.), *Scramjet Propulsion*, Progress in Astronautics and Aeronautics, AIAA, Reston, VA, 2001.

[2] Zukoski, E. E., and Spaid, F. W., "Secondary Injection of Gases into a Supersonic Flow," *AIAA Journal*, Vol. 2, No. 10, 1964, pp. 1689–1696. doi:10.2514/3.2653

[3] Schetz, J. A., and Billig, F. S., "Penetration of Gaseous Jets Injected into a Supersonic Stream," *Journal of Spacecraft and Rockets*, Vol. 3, No. 11, 1966, pp. 1658–1665. doi:10.2514/3.28721

[4] Schetz, J. A., Weinraub, R. A., and Mahaffey, R. E., Jr., "Supersonic Transverse Injection into a Supersonic Stream," *AIAA Journal*, Vol. 6, No. 5, 1968, pp. 933–934. doi:10.2514/3.4631

[5] Cohen, L. C., Coulter, L. J., and Egan, W. J., Jr., "Penetration and Mixing of Multiple Gas Jets Subjected to a Cross Flow," *AIAA Journal*, Vol. 9, No. 4, 1971, pp. 718–724. doi:10.2514/3.6253

[6] McDaniel, J. C., and Graves, J., Jr., "Laser-Induced-Fluorescence Visulaization of Transverse Gaseous Injection in a Nonreacting Supersonic Combustor," *Journal of Propulsion and Power*, Vol. 4, No. 6, 1988, pp. 591–597. doi:10.2514/3.23105

[7] Hermanson, J. C., and Winter, M., "Mie Scattering Imaging of a Transverse, Sonic Jet in Supersonic Flow," *AIAA Journal*, Vol. 31, No. 1, 1993, pp. 129–132. doi:10.2514/3.11328

[8] Gruber, M. R., Nejad, A. S., Chen, T. H., and Dutton, J. C., "Compressibility Effects in Supersonic Transverse Injection Flowfields," *Physics of Fluids*, Vol. 9, No. 5, 1997, pp. 1448–1461. doi:10.1063/1.869257

[9] Santiago, J. G., and Dutton, J. C., "Velocity Measurements of a Jet Injected into a Supersonic Crossflow," *Journal of Propulsion and Power*, Vol. 13, No. 2, 1997, pp. 264–273. doi:10.2514/2.5158

[10] Everett, D. E., Woodmansee, M. A., Dutton, J. C., and Morris, M. J., "Wall Pressure Measurements for a Sonic Jet Injected Transversely into a Supersonic Crossflow," *Journal of Propulsion and Power*, Vol. 14, No. 6, 1998, pp. 861–868. doi:10.2514/2.5357

[11] VanLerberghe, W. M., Santiago, J. G., Dutton, J. C., and Lucht, R. P., "Mixing of a Sonic Transverse Jet Injected into a Supersonic Flow," *AIAA Journal*, Vol. 38, No. 3, 2000, pp. 470–479. doi:10.2514/2.984

[12] Tomioka, S., Jacobsen, L. S., and Schetz, J. A., "Sonic Injection from Diamond-Shaped Orifices into a Supersonic Crossflow," *Journal of Propulsion and Power*, Vol. 19, No. 1, 2003, pp. 104–114. doi:10.2514/2.6086

[13] Bowesox, R. D. W., Fan, H., and Lee, D., "Sonic Injection into a Mach 5.0 Freestream Through Diamond Orifices," *Journal of Propulsion and Power*, Vol. 20, No. 2, 2004, pp. 280–287. doi:10.2514/1.9254

[14] Ben-Yakar, A., Mungal, M. G., and Hanson, R. K., "Time Evolution and Mixing Characteristics of Hydrogen And Ethylene Transverse Jets in Supersonic Crossflows," *Physics of Fluids*, Vol. 18, No. 2, 2006, Paper 026101.

[15] Sriram, A. T., and Mathew, J., "Numerical Simulation of Transverse Injection of Circular Jets into Turbulent Supersonic Streams," *Journal of Propulsion and Power*, Vol. 24, No. 1, 2008, pp. 45–54. doi:10.2514/1.26884

[16] Srinivasan, R., and Bowersox, R. D. W., "Transverse Injection Through Diamond and Circular Ports into a Mach 5.0 Freestream," *AIAA Journal*, Vol. 46, No. 8, 2008, pp. 1944–1962. doi:10.2514/1.29253

[17] Viti, V., Neel, R., and Schetz, J. A., "Detailed Flow Physics of the Supersonic Jet Interaction Flow Field," *Physics of Fluids*, Vol. 21, 2009, Paper 046101. doi:10.1063/1.3112736

[18] von Lavante, E., Zeitz, D., and Kallenberg, M., "Numerical Simulation of Supersonic Airflow with Transverse Hydrogen Injection," *Journal of Propulsion and Power*, Vol. 17, No. 6, 2001, pp. 1319–1326. doi:10.2514/2.5881

[19] Kawai, S., and Lele, S. K., "Large-Eddy Simulation of Jet Mixing in a Supersonic Turbulent Crossflow," AIAA Paper 2009-3795, June 2009.

[20] Piomelli, U., and Balaras, E., "Wall-Layer Models for Large-Eddy Simulations," *Annual Review of Fluid Mechanics*, Vol. 34, 2002, pp. 349–374. doi:10.1146/annurev.fluid.34.082901.144919

[21] Spalart, P. R., Jou, W-H., Strelets, M., and Allmaras, S. R., "Comments on the Feasibility of LES for Wings and on a Hybrid RANS/LES Approach," *Advances in DNS/LES, 1st AFOSR International Conference on DNS/LES*, Greyden, Columbus, OH, Aug. 1997.

[22] Nikitin, N. V., Nicoud, F., Wasistho, B., Squires, K. D., and Spalart, P. R., "An Approach to Wall Modeling in Large-Eddy Simulations," *Physics of Fluids*, Vol. 12, No. 7, 2000, pp. 1629–1632. doi:10.1063/1.870414

[23] Spalart, P. R., Deck, S., Shur, M. L., Squires, K. D., Strelets, M. Kh., and Travin, A., "A New Version of Detached-Eddy Simulation, Resistant to Ambiguous Grid Densities," *Theoretical and Computational Fluid Dynamics*, Vol. 20, 2006, pp. 181–195. doi:10.1007/s00162-006-0015-0

[24] Travin, A. K., Shur, M. L., Spalart, P. R., and Strelets, M. Kh., "Improvement of Delayed Detached-Eddy Simulation for LES with Wall Modelling," *Proceedings of the European Conference on Computational Fluid Dynamics ECCOMAS CFD* [CD-ROM], edited by P. Wessling, E. Onate, and J. Periaux, Egmond aan Zee, The Netherlands, 2006.

[25] Shur, M. L., Spalart, P. R., Strelets, M. Kh., and Travin, A. K., "A Hybrid RANS-LES Approach with Delayed-DES and Wall-Modelled LES Capabilities," *International Journal of Heat and Fluid Flow*, Vol. 29, No. 6, 2008, pp. 1638–1649. doi:10.1016/j.ijheatfluidflow.2008.07.001

[26] Deck, S., Garnier, E., and Guillen, P., "Turbulence Modelling Applied to Space Launcher Configurations," *Journal of Turbulence*, Vol. 3, No. 57, 2002, pp. 1–21. doi:10.1088/1468-5248/3/1/057

[27] Boles, J. A., Edwards, J. R., and Baurle, R. A., "Hybrid LES/RANS Simulation of Transverse Sonic Injection into a Mach 2 Flow," AIAA Paper 2008-622, 2008.

[28] Boles, J. A., Jung-Il, C., Edwards, J. R., and Baurle, R. A., "Simulations of High-Speed Internal Flows using LES/RANS Models," AIAA Paper 2009-1324, 2009.

[29] Nompelis, I., Drayna, T. W., and Candler, G. V., "Development of a Hybrid Unstructured Implicit Solver for the Simulation of Reacting Flows Over Complex Geometries," AIAA Paper 2004-2227, June 2004.

[30] Wright, M. J., Candler, G. V., and Prampolini, M., "Data-Parallel Lower Upper Relaxation Method for the Navier–Stokes Equations," *AIAA Journal*, Vol. 34, No. 7, 1996, pp. 1371–1377. doi:10.2514/3.13242

[31] Spalart, P. R., and Allmaras, S. R., "A One-Equation Turbulence Model for Aerodynamic Flows," AIAA Paper 1992-0439, 1992.

[32] Catris, S., and Aupoix, B., "Density Corrections for Turbulence Models," *Aerospace Science and Technology*, Vol. 4, No. 1, 2000, pp. 1–11. doi:10.1016/S1270-9638(00)00112-7

[33] Spalart, P. R., "Topics in Detached-Eddy Simulation," *International Conference on Computational Fluid Dynamics*, Springer, Berlin, July 2004, pp. 3–12.

[34] Lund, T., Wu, X., and Squires, K., "Generation of Turbulent Inflow Data for Spatially Developing Boundary Layer Simulations," *Journal of Computational Physics*, Vol. 140, No. 2, 1998, pp. 233–258. doi:10.1006/jcph.1998.5882

[35] Subbareddy, P., Peterson, D., Candler, G. V., and Marusic, I., "A Synthetic Inflow Generation Method Using the Attached Eddy Hypothesis," AIAA Paper 2006-3672, 2006.

[36] Peterson, D. M., Subbareddy, P. K., and Candler, G. V., "Assessment of Synthetic Inflow Generation for Simulating Injection Into a Supersonic Crossflow," AIAA Paper 2006-8128, 2006.
[37] Spalart, P. R., "Young-Person's Guide to Detached-Eddy Simulation Grids," NASA CR-2001-211032, July 2001.
[38] GridPro, Software Package, Ver. 4.4, Program Development Corp., White Plains, NY.
[39] Peterson, D. M., Subbareddy, P. K., and Candler, G. V., "Detached Eddy Simulations of Flush Wall Injection into a Supersonic Freestream," AIAA Paper 2006-4576, 2006.
[40] Chacin, J., and Cantwell, B., "Study of Turbulence Structure Using the Invariants of the Velocity Gradient Tensor," Report No. TF-70, Dept. of Mechanical Engineering, Stanford Univ., Stanford, CA, Aug. 1997.

J. Oefelein
Associate Editor